RSC Advances

PAPER

View Article Online
View Journal | View Issue

Cite this: *RSC Adv.*, 2025, **15**, 39203

Photodegradation of diclofenac in aqueous media *via* a HO˙ radical pathway using CeO_2/g-C_3N_4 heterojunction under visible light: experimental and computational insights

Dang Van Do, *[a] Cham Thanh Le,[a] Xoan Thi Nguyen,[a] Son Thanh Le,[a] Khai Manh Nguyen[bc] and Thi Chinh Ngo *[de]

Diclofenac (DCF), a widely prescribed nonsteroidal anti-inflammatory drug (NSAID), is frequently detected in aquatic environments due to its extensive usage and poor removal by conventional wastewater treatment technologies. Among various remediation strategies, photocatalysis has emerged as a cost-effective and sustainable approach for the degradation of such persistent pharmaceutical pollutants. In this study, a CeO_2/g-C_3N_4 heterojunction photocatalyst was synthesized and optimized for the visible-light-driven photodegradation of DCF in aqueous media. Under optimized conditions (catalyst dosage: 0.5 g L^{-1}, initial pH: 6.8, light source: 200 W Xe lamp with $\lambda > 420$ nm cutoff filter), the composite achieved 92.6% DCF removal and 75% TOC removal after 180 minutes, demonstrating both efficient degradation and substantial mineralization. The improved photocatalytic activity can be attributed to the effective separation of photogenerated charge carriers, made possible by forming a type-II heterojunction and the strong visible-light absorption capacity of the composite. Radical scavenging experiments confirmed that hydroxyl radicals (˙OH) play a dominant role in the degradation mechanism, while complementary DFT-based computational analysis provided further support by revealing a high rate constant ($k = 1.56 \times 10^{10}$ M^{-1} s^{-1}) for the HO˙–DCF reaction. The structural and optical properties of the photocatalyst were thoroughly characterized using XRD, SEM-EDX, UV-Vis DRS, and FT-IR, confirming the successful formation of the CeO_2/g-C_3N_4 heterostructure. These results highlight the practical potential of CeO_2/g-C_3N_4 for wastewater treatment and solar-driven environmental remediation, providing guidance for designing advanced photocatalytic systems targeting recalcitrant pollutants.

Received 24th August 2025
Accepted 13th October 2025

DOI: 10.1039/d5ra06295k

rsc.li/rsc-advances

1. Introduction

Persistent traces of pharmaceutical compounds, particularly nonsteroidal anti-inflammatory drugs (NSAIDs), have been extensively documented across various environmental matrices such as surface waters, sediments, and soils spanning rivers, lakes, coastal environments, and agricultural areas.[1] This widespread occurrence has raised growing concerns regarding its potential ecological and human health impacts. Among these, diclofenac (DCF), a commonly prescribed NSAID belonging to the phenylacetic acid category, is notable for its strong anti-inflammatory, analgesic, and antipyretic effects.[2] However, DCF exhibits low biodegradability, high aquatic toxicity, and a strong tendency for bioaccumulation, making it a high-risk pollutant in both aquatic and terrestrial ecosystems.[3] Consequently, there is an urgent need for advanced water treatment technologies capable of effectively degrading recalcitrant pharmaceutical pollutants.

Numerous strategies have been developed for the removal or degradation of diclofenac (DCF), a widely detected pharmaceutical contaminant in aquatic environments. These include adsorption,[4] ozonation,[5] photoelectrocatalytic degradation,[6] bioremediation,[7] and notably, photocatalytic degradation.[8–13] Among these approaches, there is increasing consensus that wastewater treatment technologies should not only be efficient and reliable but also environmentally sustainable and economically feasible.[14] In this context, photocatalytic degradation has gained significant attention as an effective approach due to its ability to fully decompose persistent organic contaminants into benign end products like carbon dioxide and

[a]Faculty of Chemistry, VNU University of Science Ha Noi, 19 Le Thanh Tong, Ha Noi, Vietnam. E-mail: dangdovan@hus.edu.vn
[b]Faculty of Environmental Sciences, VNU University of Science Ha Noi, 334 Nguyen Trai, Ha Noi, Vietnam
[c]VNU Key Laboratory of Green Environment, Technology and Waste Utilization (GreenLab), VNU University of Science Ha Noi, 334 Nguyen Trai, Ha Noi, Vietnam
[d]Institute of Research and Development, Duy Tan University, Da Nang, 550000, Vietnam. E-mail: ngothichinh@duytan.edu.vn
[e]School of Engineering and Technology, Duy Tan University, Da Nang, 550000, Vietnam

water, using only a photocatalyst and light irradiation.[15] Following light excitation, semiconductor photocatalysts produce electron–hole pairs (e^-/h^+), which drive redox processes that subsequently yield reactive oxygen species, including hydroxyl radicals (HO$^\bullet$) and superoxide anion radicals ($O_2^{\bullet-}$).[12,16,17] These reactive oxygen species are crucial in oxidizing complex organic contaminants, thereby facilitating their decomposition and enhancing overall pollutant removal efficiency.[15,18]

Graphitic carbon nitride (g-C_3N_4) has attracted significant attention as a metal-free photocatalyst owing to its moderate bandgap (~2.7 eV), robust chemical stability, and effective absorption of visible light wavelengths up to approximately 460 nm.[18] Despite these advantages, its photocatalytic efficiency is limited by the rapid recombination of photogenerated electron–hole pairs, which shortens their lifetime and compromises oxidative capability.[18] To address this limitation, heterojunction-based approaches have been widely explored. These include element doping and coupling with other semiconductors to form composites such as g-C_3N_4/TiO_2,[19] C–TiO_2/g-C_3N_4,[20] $BiMnO_3$/g-C_3N_4,[21] Fe_2O_3/g-C_3N_4/ZnO,[22] SiO_2/g-C_3N_4,[23] and $NiFe_2O_4$@P-doped g-C_3N_4,[24] thereby promoting more efficient charge carrier separation, extending light-harvesting capacity, and enriching the surface with active sites.

Cerium dioxide (CeO_2) is a redox-active rare-earth oxide semiconductor with a moderate band gap (~3.0 eV), high oxygen storage capacity, and remarkable chemical and thermal stability.[25,26] Its unique ability to undergo reversible Ce^{4+}/Ce^{3+} redox transitions and host oxygen vacancies makes it highly suitable for environmental remediation applications. CeO_2-based catalysts have shown significant activity in oxidative degradation processes, including Fenton-like reactions, where transition metal-doped CeO_2 (*e.g.*, CuO/CeO_2) has demonstrated high efficacy in DCF degradation *via* HO$^\bullet$ radical mechanisms, achieving over 80% removal under optimal conditions.[27]

Combining CeO_2 with g-C_3N_4 into a heterojunction structure offers several advantages. The alignment of their band structures promotes interfacial electron transfer, where photoexcited electrons from the conduction band of g-C_3N_4 migrate to that of CeO_2. This process suppresses charge recombination, prolongs charge carrier lifetimes, and enhances the generation of reactive oxygen species such as HO$^\bullet$ and $O_2^{\bullet-}$. Although CeO_2/g-C_3N_4 has been reported for the removal of dyes, NO, ciprofloxacin, bisphenol A, and parabens under visible or simulated sunlight,[28–35] by rationally engineering CeO_2/g-C_3N_4 S- and Z-scheme interfaces, and by introducing co-catalysts or magnetic/adsorptive components to improve charge separation and recyclability. However, despite these advances, application of binary CeO_2/g-C_3N_4 specifically to the degradation of DCF remains scarce.

Beyond material design, mechanistic understanding is critical. Computational methods have proven highly effective in uncovering oxidation mechanisms mediated by reactive radicals.[36–39] For instance, Truong *et al.*[40] combined photocatalytic experiments with density functional theory (DFT) to elucidate ciprofloxacin degradation over α-$NiMoO_4$/mpg-C_3N_4/EP under visible light. Inspired by such studies, our work integrates experimental photocatalysis with DFT to resolve the oxidative mechanism of DCF degradation over CeO_2/g-C_3N_4.

In this study, a CeO_2/g-C_3N_4 heterostructured photocatalyst was synthesized, characterized, and evaluated for the visible-light-assisted degradation of DCF in aqueous media. In addition to demonstrating high photocatalytic activity, a density functional theory (DFT) approach was employed to elucidate the mechanistic role of HO$^\bullet$ radicals in the oxidative degradation of DCF. Three representative reaction pathways-hydrogen abstraction, HO$^\bullet$ addition, and single-electron transfer-were modeled at environmental pH (6–8). To the best of our knowledge, this is the first report of a binary CeO_2/g-C_3N_4 heterojunction specifically optimized for DCF degradation that integrates experimental photocatalysis with computational pathway elucidation. This dual approach not only demonstrates the efficacy of CeO_2/g-C_3N_4 for removing an environmentally persistent pharmaceutical but also provides mechanistic insights that advance the rational design of next-generation photocatalysts for pharmaceutical pollutant remediation (Scheme 1).

2. Experimental

2.1 Materials

All reagents utilized in this work were of analytical grade and were used as received, without any additional purification. The reagents included melamine ($C_3H_6N_6$, 97.5%), cerium nitrate hexahydrate ($Ce(NO_3)_3\cdot 6H_2O$, 99.9%), *p*-benzoquinone (p-BQ), ethylenediaminetetraacetic acid (EDTA), hydrochloric acid (HCl), sodium hydroxyde (NaOH), sodium chloride (NaCl), sodium nitrate ($NaNO_3$), isopropanol (IPA), and absolute ethanol (C_2H_5OH, 96%).

2.2 Synthesis of g-C_3N_4

Graphitic carbon nitride (g-C_3N_4) was synthesized *via* thermal polymerization of melamine.[18] Specifically, melamine was heated at 550 °C for 3 h in a muffle furnace under ambient air, with a ramp rate of 5 °C min^{-1}. The obtained yellow material was subsequently ground into a fine powder using a porcelain mortar and pestle.

2.3. Synthesis of CeO_2/g-C_3N_4 composites

CeO_2/g-C_3N_4 composites were prepared through a hydrothermal method. First, g-C_3N_4 powder was dispersed in a 1 : 1 ethanol–deionized water mixture, stirred for 30 min, and then sonicated for another 30 min. A defined amount of $Ce(NO_3)_3\cdot 6H_2O$ was added to the suspension, followed by additional stirring for

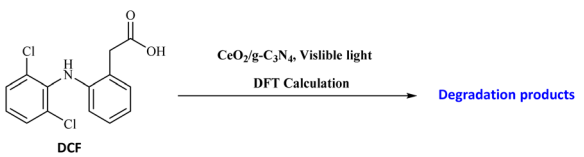

Scheme 1 Photodegradation of DCF using synthesized materials.

30 min. The reaction mixture was placed in a Teflon-lined autoclave and maintained at 160 °C for 20 hours. Upon cooling to ambient temperature, the precipitate was recovered by filtration, rinsed with deionized water and ethanol, and dried at 70 °C for 24 hours. Composites containing 10%, 15%, and 20% CeO_2 by weight were synthesized and denoted as 0.1CeO_2/g-C_3N_4, 0.15CeO_2/g-C_3N_4, and 0.2CeO_2/g-C_3N_4, respectively.

2.4. Characterization techniques

The FT-IR spectra were recorded using a Bruker ALPHA FTIR spectrometer. The UV-Visible diffuse reflectance spectra (UV-DRS) were recorded using a Hitachi UH4150 spectrophotometer equipped with an integrating sphere, with $BaSO_4$ as the reflectance standard. Powder X-ray diffraction (XRD) patterns were obtained on a PANalytical Empyrean diffractometer (Cu Kα radiation, $\lambda = 0.15406$ nm; 40 kV, 40 mA) using an X'Celerator detector. Scanning electron microscopy (SEM) was conducted using a Hitachi Regulus 8100. Elemental mapping and energy-dispersive X-ray spectroscopy (EDS) were performed using an Oxford X-stream 2 detector. Photoluminescence (PL) measurements were performed using a Horiba Fluoromax-4 fluorescence spectrometer to evaluate the optical properties of the samples. Quantitative analysis of trace elements was conducted using inductively coupled plasma mass spectrometry (ICP-MS) on an Elan 9000 (PerkinElmer).

2.5. Photocatalytic activity evaluation

Photocatalytic degradation of DCF was evaluated under visible light irradiation. In a typical experiment, 20 mg of catalyst was dispersed in 50 mL of a 10 mg L^{-1} DCF solution and stirred in the dark for 30 min to reach adsorption–desorption equilibrium, followed by irradiation with a 200 W LED lamp ($\lambda > 420$ nm). Aliquots were withdrawn at regular intervals and analyzed by UV-Vis spectrophotometry (details in SI). The effect of pH was examined within the range of 3–9, while the influence of coexisting ions (10 mM NaCl, or $NaNO_3$) was also investigated. To probe the degradation mechanism, isopropyl alcohol, *p*-benzoquinone, and EDTA were employed as scavengers for HO˙, $O_2^{\cdot-}$, and h^+, respectively. A control experiment confirmed negligible photolysis of DCF in the absence of catalyst, and the reusability of the CeO_2/g-C_3N_4 composite was examined over successive cycles. Degradation efficiency and reaction kinetics were calculated according to eqn (1) and (2), respectively. Mineralization was further assessed by TOC analysis (eqn (3)). For practical validation, wastewater samples collected from Hoan Kiem Lake (21.028889 °N, 105.8525 °E) and the To Lich river (21.0042 °N, 105.8209 °E), Ha Noi, Viet nam were treated under the same photocatalytic protocol, and TOC measurements before and after irradiation confirmed the extent of mineralization.

$$\%\text{Removal} = \frac{C_0 - C_t}{C_0} \times 100 \quad (1)$$

$$\ln\frac{C_0}{C_t} = kt \quad (2)$$

$$\%\text{TOC removal} = \frac{\text{TOC}_0 - \text{TOC}_t}{\text{TOC}_0} \times 100 \quad (3)$$

2.6. Computational methods

The Gaussian 16 Rev.C.01 package was used for all calculations.[41] The structural optimization and frequency calculations are performed by Minnesota M06-2X[42] functional combined with a 6–31 + G(d,p) basis set. A high 6–311++G(3df,3pd) level of theory is then applied to estimate single-point energies. The calculations in the aqueous phase are performed by the solvation model based on the quantum mechanical charge density of a solute molecule interacting with a continuum description of the solvent (SMD). Three reactions, including hydrogen abstraction (Abs), addition (Add), and single electron transfer (SET) between the studied compounds and HO˙-radical, are investigated. A computational method for calculating the rate constants of these reactions is detailed in the SI (File).

The overall rate constant ($k_{overall}$) is the total of all rate constants from the component reactions. The branching ratios (Γ_i) for each reaction are calculated by dividing the apparent rate constants (k_i) by the $k_{overall}$.

3. Results and discussions

3.1 Material characterization

The crystalline structures of CeO_2, g-C_3N_4, and their composites were analyzed by powder X-ray diffraction (XRD), as shown in Fig. 1. The XRD pattern of pristine g-C_3N_4 exhibited characteristic peaks at 27.4°, corresponding to the (002) crystal planes, respectively.[18] These reflections are associated with the in plane repeating units and interlayer stacking of the graphitic structure. The diffraction peaks of CeO_2 appeared at 28.5°, 32.9°, 47.4°, 56.2°, 59.1°, 69.3°, 77.1°, and 78.9°, corresponding to the (111), (200), (220), (311), (222), (400), (331), and (420) crystal planes of the fluorite cubic structure (JCPDS No. 34-0394).[43] The

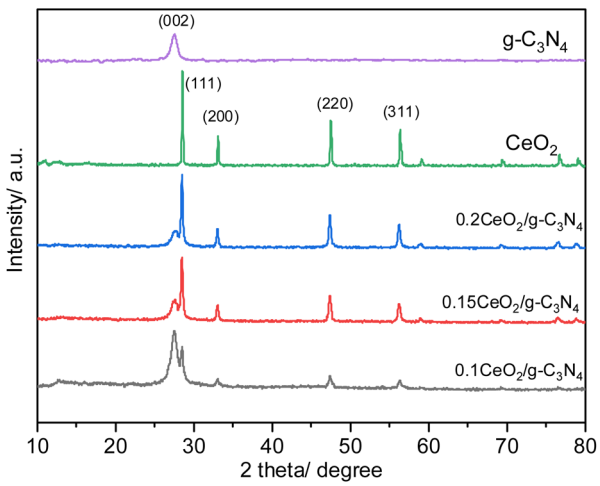

Fig. 1 XRD result of g-C_3N_4, CeO_2, 0.1CeO_2/g-C_3N_4, 0.15CeO_2/g-C_3N_4, and 0.2CeO_2/g-C_3N_4.

XRD patterns of the CeO_2/g-C_3N_4 composites displayed characteristic peaks from both components, confirming the successful incorporation of CeO_2 into the g-C_3N_4 framework. With increasing CeO_2 content from 10% to 20%, the intensities of CeO_2 peaks gradually increased, while those of g-C_3N_4 diminished, indicating progressive incorporation of CeO_2 into the composite structure.

To further validate the formation of the CeO_2/g-C_3N_4 heterostructure, FT-IR spectroscopy was conducted and shown in Fig. S1 of the SI. The FT-IR spectrum of pure g-C_3N_4 exhibited a broad absorption band between 3000 and 3500 cm^{-1}, attributable to O–H stretching and N–H or NH_2 functional groups. A distinct peak at 1645 cm^{-1} corresponded to C=N stretching vibrations in the heptazine units. Additional peaks at 1569, 1461, 1411, 1320, and 1241 cm^{-1} were assigned to C–N stretching in the aromatic framework, while the band at 810 cm^{-1} was linked to the out-of-plane bending of C–N heterocycles.[18] Notably, the absorption bands of CeO_2/g-C_3N_4 composites remained, further confirming successful hybridization. No additional absorption bands attributable to Ce–O stretching (typically observed in the 400–700 cm^{-1} range) or consistent shifts of the g-C_3N_4 framework vibrations were detected. This indicates that interfacial Ce–O–N bonding is either IR-inactive or below the detection limit of the technique. Evidence for the intimate contact between CeO_2 and g-C_3N_4 is instead provided by SEM–EDX elemental mapping, which demonstrates a homogeneous distribution of Ce and O in the composite material.

SEM was utilized to investigate the surface morphologies of the individual components and the CeO_2/g-C_3N_4 composite samples (Fig. S2, SI). Pristine CeO_2 consisted of aggregated nanoparticles with an average equivalent diameter of 2.0 ± 1.5 μm (range: 0.8–8.8 μm), while g-C_3N_4 exhibited the expected layered nanosheet morphology with lateral dimensions of 190 ± 386 nm (range: 35–1560 nm). In contrast, the CeO_2/g-C_3N_4 composites revealed a more uniform and homogeneous distribution of CeO_2 nanoparticles across the g-C_3N_4 nanosheets, indicating successful integration and interfacial contact between the two components. This improved dispersion is expected to facilitate effective charge transfer and interfacial interaction. Additionally, energy-dispersive X-ray spectroscopy (EDX) analysis verified the elemental composition and distribution of Ce, C, N, and O within the composite. The elemental mapping results, presented in Fig. S3 of the SI, further validate the successful incorporation and uniform dispersion of CeO_2 within the g-C_3N_4 matrix.

To investigate the optical properties and electronic band structures of the synthesized materials, UV-Vis diffuse reflectance spectroscopy (DRS) was performed, as shown in Fig. S4 of the SI. All samples demonstrated pronounced absorption within the visible spectrum, with absorption edges ranging from approximately 420 to 540 nm. The optical band gap energies were determined from Tauc plots (Fig. S4, SI), revealing a slight increase from 2.66 eV to 2.69 eV as the CeO_2 content increased. This minor shift is insufficient to explain the pronounced enhancement in photocatalytic performance. Instead, the improvement is primarily ascribed to the heterojunction formed between CeO_2 and g-C_3N_4, which facilitates efficient charge separation and interfacial charge transfer. Furthermore, to confirm the recombination behavior of photogenerated electron–hole pairs, PL spectra were recorded for g-C_3N_4, CeO_2, and the CeO_2/g-C_3N_4 composites (Fig. S5, SI). The PL intensities follow the trend g-C_3N_4 > 0.1CeO_2/g-C_3N_4 > 0.2CeO_2/g-C_3N_4 > 0.15CeO_2/g-C_3N_4 > CeO_2, indicating that charge recombination decreases progressively with CeO_2 loading and is lowest for 0.15CeO_2/g-C_3N_4. Pristine g-C_3N_4 exhibits high PL intensity, reflecting significant electron–hole recombination, whereas the formation of the CeO_2/g-C_3N_4 heterojunction facilitates more efficient charge separation. The progressive quenching of emission intensity with increasing CeO_2 content further confirms the suppression of electron–hole recombination. Notably, the slightly higher PL of 0.2CeO_2/g-C_3N_4 compared to 0.15CeO_2/g-C_3N_4 suggests that excessive CeO_2 may cause particle agglomeration and partial surface coverage, limiting light penetration and reducing the effective active surface area, which aligns with the observed marginal decline in photocatalytic performance.

3.2 Degradation of DCF

The catalytic performance of the synthesized materials was assessed through photocatalytic degradation tests employing diclofenac (DCF) as a representative pollutant. All reactions were performed under identical conditions: 10 mg L^{-1} initial DCF concentration, 20 mg of photocatalyst (0.4 g L^{-1}), and 180 minutes of visible light irradiation. Adsorption equilibrium in the dark was established before irradiation, as the DCF concentration remained stable after 30 minutes. Control experiments performed under light irradiation in the absence of any photocatalyst confirmed negligible DCF degradation, highlighting the essential role of the catalyst in driving the photocatalytic process. The photocatalytic performance of pristine g-C_3N_4, CeO_2, and CeO_2/g-C_3N_4 composites with different CeO_2 loadings was compared, as shown in Fig. 2. Pure

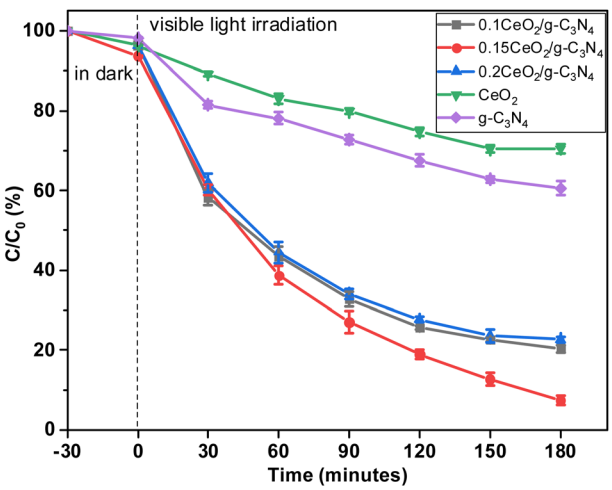

Fig. 2 Photodegradation of DCF using g-C_3N_4, CeO_2, 0.1CeO_2/g-C_3N_4, 0.15CeO_2/g-C_3N_4, and 0.2CeO_2/g-C_3N_4 catalysts.

g-C_3N_4 and CeO_2 demonstrated moderate degradation efficiencies of 39.5% and 29.5%, respectively, after 180 minutes of irradiation. In contrast, the CeO_2/g-C_3N_4 catalysts exhibited enhanced DCF degradation efficiencies of 79.6%, 92.6%, and 77.3% for 0.1CeO_2/g-C_3N_4, 0.15CeO_2/g-C_3N_4, and 0.2CeO_2/g-C_3N_4, respectively, highlighting the synergistic effect of heterojunction formation. Despite having the lowest band gap (2.66 eV), 0.1CeO_2/g-C_3N_4 showed a moderate efficiency (79.6%), likely due to CeO_2 acting as a recombination center, limiting ROS formation. The superior performance of 0.15CeO_2/g-C_3N_4 is attributed to optimal CeO_2 loading, which maximizes charge separation, as supported by PL spectra following the trend g-C_3N_4 > 0.1CeO_2/g-C_3N_4 > 0.2CeO_2/g-C_3N_4 > 0.15CeO_2/g-C_3N_4 > CeO_2, indicating the lowest electron–hole recombination (Fig. S5, SI). The slight decline in 0.2CeO_2/g-C_3N_4 efficiency results from excessive CeO_2 loading, causing particle agglomeration and surface coverage, which reduce light penetration, active surface area, and interactions with DCF. Accordingly, 0.15CeO_2/g-C_3N_4 was selected for all subsequent photocatalytic investigations.

To gain deeper insight into the reaction kinetics of DCF photodegradation catalyzed by CeO_2/g-C_3N_4, the experimental results were fitted to a pseudo-first-order kinetic model (eqn (2)). As illustrated in Fig. S6 (SI), a linear correlation between $\ln(C_0/C)$ and irradiation time confirmed that the photodegradation of DCF over all tested catalysts followed pseudo-first-order kinetics, and the corresponding apparent rate constants (k) were also derived. A distinct increase in the rate constant was observed with the progressive augmentation of CeO_2 content on the g-C_3N_4 surface. Among the series, 0.15CeO_2/g-C_3N_4 exhibited the highest apparent rate constant (k = 0.0131 min^{-1}), demonstrating competitive and efficient performance under realistic conditions (10 mg L^{-1} DCF, visible LED irradiation, without external oxidants), as summarized in Table 1.

Catalyst dosage is a key factor in optimizing photocatalytic efficiency. The impact of varying catalyst loadings (0.2–0.6 g L^{-1}) on DCF degradation using the 0.15CeO_2/g-C_3N_4 catalyst is presented in Fig. S6 (SI). Increasing the catalyst concentration from 0.2 to 0.4 g L^{-1} led to improved degradation efficiency, largely attributed to the greater number of active sites and the elevated production of reactive species, including hydroxyl radicals and photogenerated holes.

Nonetheless, a further increase beyond 0.4 g L^{-1} resulted in a marginal decrease in photocatalytic performance. This reduction is likely due to catalyst particle agglomeration and excessive surface coverage, which hinder light penetration and Earlier studies have demonstrated that pH exerts minimal influence on diclofenac (DCF) removal over an extensive pH range (3.00 to 9.00).[44] The modest and statistically insignificant improvement in DCF degradation observed under acidic conditions is mainly ascribed to electrostatic interactions between the catalyst surface and the substrate. The effect of pH on the process exhibits greater complexity in systems utilizing heterogeneous catalysts, as pH can alter their physicochemical properties, consistent with previous studies.[45,46] In the present study, the initial pH adjustment led to only slight changes in DCF photodegradation efficiency. Considering that the pHPZC of CeO_2/g-C_3N_4 is 6.7 (Fig. S8, SI), the catalyst surface is positively charged at pH < 6.7 and negatively charged at pH > 6.7, while DCF exists mainly in its anionic form at pH above its pK_a ($\approx$4.25). Therefore, electrostatic interactions between the negatively charged DCF and the catalyst surface likely explain the slightly enhanced removal under acidic conditions, while at higher pH, repulsion reduces this effect.

To confirm the degradation pathway of DCF, total organic carbon (TOC) was measured before and after photocatalytic treatment (Fig. S9, SI). The TOC removal reached 29.9% after 60 min and increased to 75% after 180 min, demonstrating substantial mineralization of DCF under prolonged irradiation and confirming that the catalyst enables not only DCF degradation but also effective diminish the effective active surface area. These findings are supported by the kinetic analysis shown in Fig. S7 (SI), where the 0.4 g L^{-1} catalyst dosage yielded the highest apparent rate constant, confirming it as the optimal loading for this system.

Table 1 Comparative summary of photocatalytic degradation performance for DCF using various photocatalysts[a]

Catalyst	Light sourse	Diclofenac concentration	Catalyst concentration	Reaction time (min)	Degradation efficiency (%)	Apparent first-order rate constant	Recyle ability	Ref.
Ag–BiOI-rGO	300 w halogen	10 mg L^{-1}	1 g L^{-1}	80	99.0	0.026 min^{-1}	3	12
CNQD	300 W Xenon	20 mg L^{-1}	1.0 g L^{-1}	180	62.0	0.0054 min^{-1}	n.r.	8
g-C_3N_4/$BiVO_4$	n.r.	10 mg L^{-1}	n.r.	120	29.4	0.0032 min^{-1}	n.r.	6
Ag_3PO_4/g-C_3N_4	300 W xenon	1 mg L^{-1}	0.1 g L^{-1}	15	n.r.	0.453 min^{-1}	5	9
MoO_3@ZrO_2	500 W LED	10 mg L^{-1}	0.25 g L^{-1}	150	90.94	0.035 min^{-1}	n.r.	13
Porous carbon nitride	300 W xenon	100 mg L^{-1}	2.04 mg cm^{-2}	240	47.0	0.0049 min^{-1}	5	10
g-C_3N_4/TiO_2	Sunlight	20 mg L^{-1}	0.6 g L^{-1}	240	73.0	n.r	n.r.	11
CeO_2/g-C_3N_4	200 W LED	10 mg L^{-1}	0.4 g L^{-1}	180	91.4	0.0131 min^{-1}	5	This study[b]

[a] Continuous-flow condition. [b] DFT calculation was performed; n.r.: not reported.

Additional experiments were performed to evaluate the effect of coexisting ions (NaCl or $NaNO_3$, 10 mM) on the photocatalytic degradation of DCF over 0.15 CeO_2/g-C_3N_4. As shown in Fig. S9 (SI), the presence of these ions slightly reduced both DCF and TOC removal. This decrease can be attributed to competitive adsorption on the catalyst surface and the scavenging of HO˙ radicals by the anions.[47] Specifically, NO_3^- can react with HO˙ radicals, reducing their availability for DCF degradation, while Cl^- reacts with HO˙ to form $HOCl^{\bullet -}$ radicals, which are less reactive than free HO˙ radicals, thereby slowing the degradation rate. Quantitatively, DCF removal decreased from 92.6% (no ions) to 82.4% with NaCl and 85.7% with $NaNO_3$, while TOC removal decreased from 75% (no ions) to 66.7% with NaCl and 71.4% with $NaNO_3$.

To identify the dominant reactive species involved in the visible-light-driven photodegradation of DCF using the 0.15CeO_2/g-C_3N_4 photocatalyst, scavenging experiments were conducted and presented in Fig. 3. Notably, the photodegradation efficiency of DCF decreased drastically from 92.6% to 42% after the addition of p-BQ, indicating a critical role of $O_2^{\bullet -}$ in the degradation mechanism. A significant reduction was also observed in the presence of IPA, confirming the contribution of HO˙. Conversely, the presence of EDTA had a negligible effect on the photodegradation performance, suggesting that photogenerated holes do not substantially participate in the formation of reactive oxygen species under the given experimental conditions. In addition, photogenerated electrons (e^-) in the conduction band of CeO_2/g-C_3N_4 contribute indirectly to DCF degradation by reducing oxygen molecules to $^{\bullet}O_2^-$, which subsequently participate in oxidative degradation.

To better understand the role of hydroxyl radicals in the photocatalytic process, DFT calculations were conducted. These calculations provided the optimized geometries and electronic properties of the species involved, offering a theoretical basis for understanding the radical formation and reactivity mechanisms.

3.2.1 Optimized structure and electronic properties calculated by DFT. In an aqueous solution, the deprotonation of the –COOH group of DCF, which is an acidic compound, is considered. The molar fraction of neutral and anionic DCF in water at different pH (0–14) values is presented in Fig. S10 in the SI file. With a pK_a of about 4.2,[48] DCF exists entirely in the anionic form at environmental pH values of 6 to 8. This form is therefore considered in this study.

The optimized structure, electrostatic potential (ESP) maps, highest occupied molecular orbital (HOMO), and lowest unoccupied molecular orbital (LUMO) distribution of the anionic DCF are shown in Fig. S11 in the SI file.

The ESP map describes the charge distribution on the molecule, which shows the highly negative charge region (in red) in the carboxyl group, and other areas exhibit more positive charges. The HOMO is found throughout the molecule, showing the ability to donate electrons when reacting with free radicals. LUMO is mainly distributed around the ring connected with chlorine atoms, where the molecule can accept electrons.

3.2.2 Mechanisms and kinetics of HO˙-initiated oxidative reactions of diclofenac. Three possible reactions of HO˙ radical and the anionic form of diclofenac, including abstraction (Abs), addition (Add), and single electron transfer (SET), were investigated using the DFT method. The Abs reactions are calculated at C–H and C–Cl positions, while Add ones are performed at unsaturated C=C aromatic rings, C6 to C19 positions. The Gibbs free energy of reaction ($\Delta_r G^0$) and Gibbs free energy of activation ($\Delta G^{\neq}$) calculated at 298.15 K for all reactions are described in Fig. 4. Cartesian coordinates and optimized geometries of the transition states (TS) and products (P) for Abs and Add reactions are displayed in Tables S1 and S2 in the SI file.

Notably, the reactions involving the HO˙-radical are thermodynamically favorable, with negative $\Delta_r G^0$ values ranging from −36.25 to −2.62 kcal mol^{-1}. In contrast, the Cl-abstraction reaction is unfavorable, exhibiting a positive value of 36.51 kcal mol^{-1} (Fig. 4). Two of the most negative values, −36.25 and −35.01 kcal mol^{-1}, are assigned to the Add-C14 and Add-C15 reactions, where the addition of HO˙ radical to molecules results in C–Cl breaking bonds. In addition, Abs-H20 and Abs-H21 showed the greatest negative $\Delta_r G^0$ values of −33.09 and −32,84 kcal mol^{-1} among Abs reactions (Fig. 4).

Regarding kinetics, the $\Delta G^{\neq}$ of the SET reaction is relatively low at 0.80 kcal mol^{-1}, resulting in a high-rate constant of 8.35 × 10^9 M^{-1} s^{-1} (Table S3). The Add-C11 and Add-C12 reactions are also kinetically favorable, with $\Delta G^{\neq}$ values of 5.47 and 5.31 kcal mol^{-1}, and their rate constants are also high, at 2.01 × 10^9 and 2.28 × 10^9 M^{-1} s^{-1}. In the Abs reaction, the barrier energy of Abs-Cl remains high at 44.97 kcal mol^{-1}. The H-abstraction from the benzylic positions (*i.e.,* Abs-H20 and Abs-H21) is more thermodynamically and kinetically favorable than the ones from the rings. This aligns with previous studies[49,50] and can be explained by the stabilization provided by the conjugation of the benzylic radical. These two reactions displayed rate constants of 1.20 × 10^8 and 3.59 × 10^8 M^{-1} s^{-1} (Table S3).

The overall rate constant for the reaction between HO˙ and anionic DCF is notably high at 1.56 × 10^{10} M^{-1} s^{-1} representing

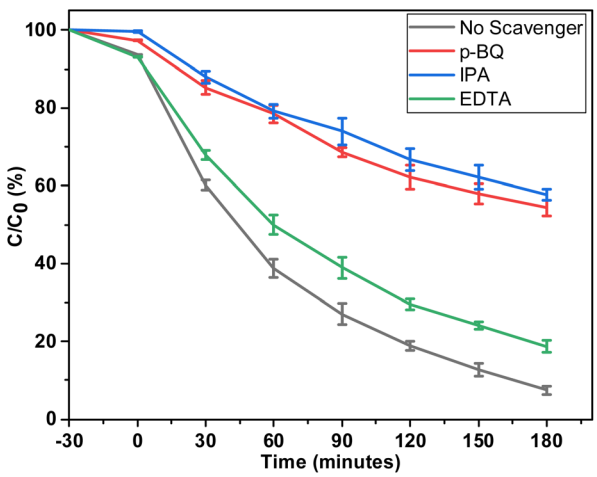

Fig. 3 Impact of different scavenging agents on the photocatalytic degradation of DCF on 0.15CeO_2/g-C_3N_4.

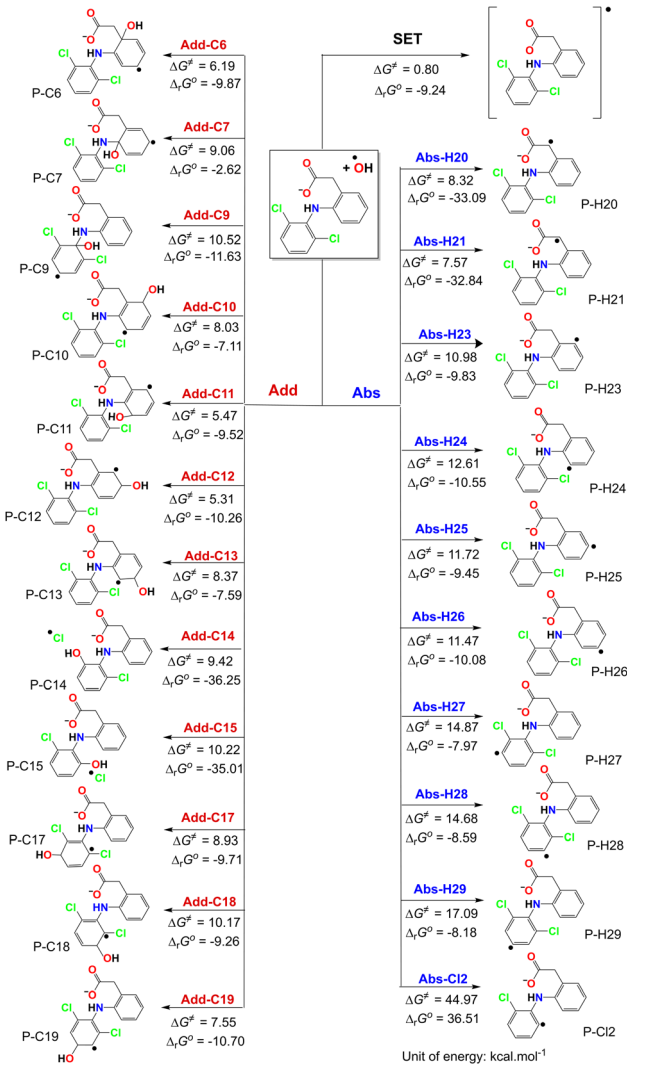

Fig. 4 Degradation pathways of anionic DCF by HO$^{\bullet}$radicals, Gibbs free energies of reaction (Δ_rG^0), and Gibbs free energies of activation ($\Delta G^{\neq}$) calculated at 298.15 K in water.

a theoretical value rather than an experimentally determined kinetic constant in this work. The dominant contribution comes from the SET reaction at 53.56%, while the additional reactions account for 43.32%. Among the additional reactions, Add-C6 (10.81%), Add-C11 (12.93%), and Add-C12 (14.66%) are the main pathways. The abstraction reactions contribute the least to DCF oxidation at 3.12%. It is worth noting that the rate constant for HO$^{\bullet}$ driven degradation of DCF in aqueous media is higher than that of several compounds (dimetridazole, $k = 4.32 \times 10^9$ M^{-1} s^{-1}; ornidazole, $k = 4.42 \times 10^9$ M^{-1} s^{-1}; quinmerac, $k = 4.66 \times 10^8$ M^{-1} s^{-1}; chlorpyrifos, $k = 4.76 \times 10^8$ M^{-1} s^{-1}),[36–38] and is comparable to fenpyrazamine ($k = 1.67 \times 10^{10}$ M^{-1} s^{-1}).[39]

Drawing on the experimental findings, a proposed charge transfer pathway underlying the visible-light-induced photodegradation of DCF by the CeO_2/g-C_3N_4 photocatalyst is depicted in Fig. 5. The suggested charge transfer mechanism between the offset-band semiconductors is corroborated by the findings from reactive species quenching experiments. The electronic band structure of the CeO_2/g-C_3N_4 heterojunction was constructed by the alignment of the conduction and valence band edges of each constituent semiconductor, which were determined from UV-DRS data and calculated using eqn (4) and (5):

$$E_{CB} = \chi - E_C - \frac{1}{2}E_g \quad (4)$$

$$E_{VB} = E_g + E_{CB} \quad (5)$$

In these calculations, E_{CB} and E_{VB} denote the conduction and valence band edge potentials, respectively. The absolute electronegativity (χ) of the semiconductor, calculated as the geometric mean of the electronegativities of its constituent atoms, is 5.56 eV for CeO_2 (ref. 51–53) and 4.72 eV for g-C_3N_4.[54] E_g represents the band gap energy, while E_C is the standard energy of free electrons on the hydrogen scale (4.5 eV).[51–54] Using a band gap of 2.96 eV for CeO_2 and 2.6 eV for g-C_3N_4, the conduction and valence band edge potentials for CeO_2 are determined to be −0.44 eV and 2.54 eV, respectively, while the corresponding values for g-C_3N_4 are −1.08 eV and 1.52 eV. The relative positions of these band edges form a staggered (Type-II) heterojunction, promoting efficient charge separation as electrons migrate from the CB of g-C_3N_4 to the CB of CeO_2, while holes move from the VB of CeO_2 to the VB of g-C_3N_4, ruling out both Type-I (straddling) and Type-III (broken-gap) alignments. This band alignment is consistent with the findings of the scavenger tests, which demonstrated that the photogenerated holes in the VB of CeO_2 have adequate oxidative potential to produce hydroxyl radicals (E_{VB} of CeO_2 = +2.54 eV > E°(HO$^{\bullet}$/H_2O) = +2.20 eV), while the conduction band electrons of g-C_3N_4 possess sufficient reductive potential to thermodynamically convert molecular oxygen into superoxide radicals (E_{CB} of g-C_3N_4 = −1.04 eV < E°(O_2/$O_2^{\bullet-}$) = −0.33 eV). These results confirm that the staggered band alignment facilitates effective charge separation and transfer, facilitating the production of reactive oxygen species and enhancing the effective photodegradation of DCF under visible light exposure.

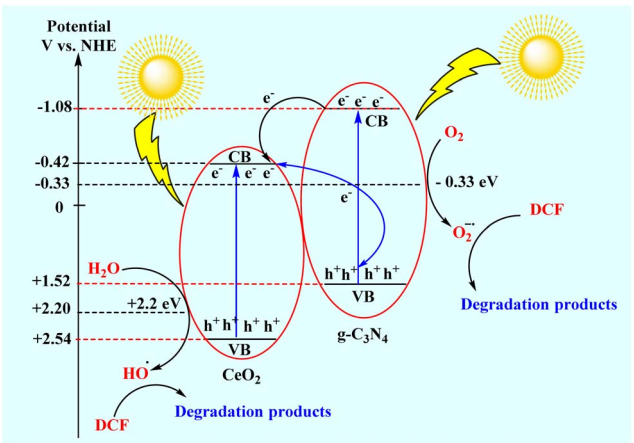

Fig. 5 A proposed mechanism diagram of DCF photodegradation on 0.15CeO_2/g-C_3N_4.

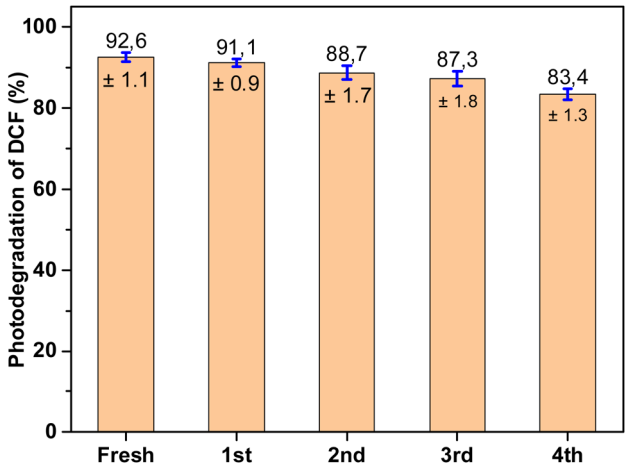

Fig. 6 Recyclability test of DCF photodegradation over 0.15CeO_2/g-C_3N_4 under visible light irradiation.

The recyclability and long-term stability of the 0.15CeO_2/g-C_3N_4 photocatalyst were investigated through repeated photodegradation cycles of diclofenac (DCF) under visible light irradiation. As shown in Fig. 6, the photocatalytic performance of 0.15CeO_2/g-C_3N_4 remained consistently high over five consecutive cycles, with no significant decline in degradation efficiency. Moreover, ICP analysis of the reaction solution detected no Ce leaching, while XRD patterns retained all characteristic diffraction peaks (Fig. S11 in SI), albeit with a moderate decrease in intensity, indicating partial loss of crystallinity but preservation of the overall structural framework. These findings confirm the excellent structural integrity and durability of the 0.15CeO_2/g-C_3N_4 photocatalyst, highlighting its strong potential for practical implementation in industrial-scale wastewater treatment applications.

To further demonstrate practical applicability, the photocatalytic activity of CeO_2/g-C_3N_4 was evaluated using wastewater samples collected from Hoan Kiem Lake (21.028889 °N, 105.8525 °E) and the To Lich river (21.0042 °N, 105.8209 °E), Ha Noi, Viet Nam. Owing to the complexity of the wastewater composition, direct quantification of diclofenac was not feasible; thus, TOC analysis was employed as an alternative measure of mineralization. The catalyst achieved TOC removal efficiencies of 61.3% and 71.3% in the respective samples, respectively, confirming its effectiveness in complex wastewater environments and highlighting its potential for practical applications.

4 Conclusion

In this work, CeO_2/g-C_3N_4 heterojunction photocatalysts were successfully synthesized and exhibited enhanced visible-light activity due to improved charge separation and interfacial electron transfer. The optimized composite achieved 92.6% removal of DCF and 75% TOC removal after 180 minutes under visible light, demonstrating not only efficient degradation but also substantial mineralization of the pollutant. The photocatalyst maintained high stability over five consecutive recycling runs, highlighting its excellent reusability. Mechanistic studies indicated that DCF degradation occurred predominantly *via* reactive oxygen species ($O_2^{\bullet-}$ and HO$^\bullet$), with computational analysis revealing the key role of HO$^\bullet$: single-electron transfer contributed 53.56% of the pathway, followed by addition (43.32%) and hydrogen abstraction (3.12%). These results underscore the strong potential of CeO_2/g-C_3N_4 for practical environmental applications, including wastewater treatment and solar-driven pollutant removal. Future work could focus on further optimizing the heterojunction structure, evaluating activity against a broader range of contaminants, and testing performance in large-scale or real-world settings.

Author contributions

Dang Van Do and Thi Chinh Ngo desired the idea and wrote the main manuscript text; Cham Thanh Le and Xoan Thi Nguyen performed experiments and drafted the manuscript; Khai Manh Nguyen, Son Thanh Le characterized physical technique and prepared figures, tables, and SI. All authors reviewed the manuscript.

Conflicts of interest

There are no conflicts to declare.

Data availability

Data which are reported in this manuscript are available from the authors upon reasonable request.

The datasets supporting this article have been uploaded as part of the supplementary information (SI). Supplementary information is available. See DOI: **https://doi.org/10.1039/d5ra06295k**.

Acknowledgements

This research has been done under the research project QG.23.13 of Vietnam National University, Hanoi. SEAGrid (**http://www.seagrid.org**)[55–57] is acknowledged for computational resources and services for the selected results used in this publication.

References

1 T. aus der Beek, F. A. Weber, A. Bergmann, S. Hickmann, I. Ebert, A. Hein and A. Küster, *Environ. Toxicol. Chem.*, 2016, **35**, 823–835.
2 R. Reis, R. Dhawle, R. Girard, Z. Frontistis, D. Mantzavinos, P. de Witte, D. Cabooter and D. Du Pasquier, *J. Hazard. Mater.*, 2024, 134458.
3 H. Yu, E. Nie, J. Xu, S. Yan, W. J. Cooper and W. Song, *Water Res.*, 2013, **47**, 1909–1918.
4 B. N. Bhadra, I. Ahmed, S. Kim and S. H. Jhung, *Chem. Eng. J.*, 2017, **314**, 50–58.

5 N. F. F. Moreira, C. A. Orge, A. R. Ribeiro, J. L. Faria, O. C. Nunes, M. F. R. Pereira and A. M. T. Silva, *Water Res.*, 2015, **87**, 87–96.
6 J. Sun, Y. Guo, Y. Wang, D. Cao, S. Tian, K. Xiao, R. Mao and X. Zhao, *Chem. Eng. J.*, 2018, **332**, 312–320.
7 C. Escapa, T. Torres, T. Neuparth, R. N. Coimbra, A. I. García, M. M. Santos and M. Otero, *Sci. Total Environ.*, 2018, **640–641**, 1024–1033.
8 H. Awang, T. Peppel and J. Strunk, *Catalysts*, 2023, **13**, 735.
9 W. Zhang, L. Zhou, J. Shi and H. Deng, *Catalysts*, 2018, **8**, 45.
10 T. Shojaeimehr, M. Tasbihi, A. Acharjya, A. Thomas, R. Schomäcker and M. Schwarze, *J. Photochem. Photobiol., A*, 2020, **388**, 112182.
11 J. A. F. Batista, J. Mendes, W. E. Moretto, M. S. Quadro, J. H. Z. dos Santos and C. C. de Escobar, *J. Environ. Chem. Eng.*, 2024, **12**, 113016.
12 W. Li, R. Yu, M. Li, N. Guo, H. Yu and Y. Yu, *Chemosphere*, 2019, **218**, 966–973.
13 G. A. Ashraf, R. T. Rasool, R. U. Rasool, M. F. Saleem, J. Ali, D. Ghernaout, M. Hassan, A. M. Aljuwayid, M. A. Habila and H. Guo, *J. Water Proc. Eng.*, 2023, **51**, 103435.
14 Y. Yang, X. Li, C. Zhou, W. Xiong, G. Zeng, D. Huang, C. Zhang, W. Wang, B. Song, X. Tang, X. Li and H. Guo, *Water Res.*, 2020, **184**, 116200.
15 V. H. Huong, T. C. Nguyen, C. D. Sai, N. H. Pham, A. B. Ngac, T. B. Nguyen, H. Van Bui, V. P. Vu, B. T. Nguyen, L. Van Dang, T. T. H. Le, T. T. Nguyen and D. Van Do, *ChemNanoMat*, 2023, **9**(6), e202300080.
16 I. Kim and H. Tanaka, *Environ. Int.*, 2009, **35**, 793–802.
17 M. Mehrali-Afjani, A. Nezamzadeh-Ejhieh and H. Aghaei, *Chem. Phys. Lett.*, 2020, **759**, 137873.
18 H. T. T. Duong, M. T. P. Duong, O. K. Nguyen, S. T. Le, L. V. Dang, B. T. Nguyen and D. V. Do, *J. Anal. Methods Chem.*, 2022, 5531219.
19 C. Q. Ruan, W. Zhang, M. Zhao, L. Hua, N. Li and K. Zeng, *Postharvest Biol. Biotechnol.*, 2025, **230**, 113774.
20 C. hui Hu, J. Hu, H. yin Liu, K. Han, H. kun Xu and F. peng Jiao, *J. Alloys Compd.*, 2025, **1036**, 181809.
21 P. Hemmati-Eslamlu, A. Habibi-Yangjeh and A. Khataee, *Surf. Interfaces*, 2025, **72**, 106922.
22 K. Wannakan, S. Nonthing, A. Panchakeaw and S. Nanan, *Diamond Relat. Mater.*, 2025, **155**, 112316.
23 T. Ranganathan and I. Selwynraj Arunodayaraj, *J. Indian Chem. Soc.*, 2024, **101**, 101371.
24 N. Bhuvaneswari, M. Arulmathi, V. P. Muralidharan, S. F. Sahlevani, F. Herrera, J. R. Joshua and M. P. Kumar, *Surf. Interfaces*, 2025, **72**, 106952.
25 A. A. Fauzi, A. A. Jalil, N. S. Hassan, F. F. A. Aziz, M. S. Azami, I. Hussain, R. Saravanan and D. V. N. Vo, *Chemosphere*, 2021, 131651.
26 J. Iqbal, N. S. Shah, Z. U. H. Khan, M. Rizwan, B. Murtaza, F. Jamil, A. Shah, A. Ullah, Y. Nazzal and F. Howari, *J. Water Proc. Eng.*, 2022, **49**, 103130.
27 J. Zhu, G. Zhang, G. Xian, N. Zhang and J. Li, *Front. Chem.*, 2019, **7**, 495180.
28 M. Zografaki, S. Stefa, I. Vamvasakis, G. S. Armatas, A. G. Chaidali, I. N. Lykakis and V. Binas, *J. Photochem. Photobiol., A*, 2025, **458**, 115976.
29 D. Meng, L. Wang, C. Zhong, J. Fu, X. Hu, D. Gao, Q. Guo, J. Hou and H. Zhao, *J. Water Proc. Eng.*, 2025, **71**, 107348.
30 A. Alsulmi, N. N. Mohammed, M. M. Hassan, M. A. Eltawil, A. E. Amin, M. Fahmy, A. Sultan and M. A. Ahmed, *Colloids Surf., A*, 2024, **689**, 133683.
31 Q. D. Ho, V. D. Lai, Q. A. Nguyen, D. N. Vu, T. K. L. Dang and D. D. La, *Diamond Relat. Mater.*, 2025, **157**, 112484.
32 Z. Chu, J. Li, Y. P. Lan, C. Chen, J. Yang, D. Ning, X. Xia and X. Mao, *Ceram. Int.*, 2022, **48**, 15439–15450.
33 H. M. Elmehdi, S. Begum, K. Ramachandran, B. Malathi, K. Hasan, R. A. Al-Qawasmeh and I. A. Shehadi, *J. Water Proc. Eng.*, 2025, **77**, 108320.
34 L. S. Alqarni, A. A. Alharbi, M. A. Ben Aissa and A. Modwi, *J. Indian Chem. Soc.*, 2025, **102**, 102129.
35 Z. Xiao, H. Do, A. Yusuf, H. Jia, H. Ma, S. Jiang, J. Li, Y. Sun, C. Wang, Y. Ren, G. Z. Chen and J. He, *J. Hazard. Mater.*, 2024, **462**, 132744.
36 J. Yao, Y. Tang, Y. Zhang, M. Ruan, W. Wu and J. Sun, *J. Hazard. Mater.*, 2022, **422**, 126930.
37 T. C. Ngo, S. Taamalli, Z. Srour, V. Fèvre-Nollet, A. El Bakali, F. Louis, I. Černušák and D. Q. Dao, *J. Environ. Chem. Eng.*, 2023, **11**, 109941.
38 D. H. Truong, T. L. A. Nguyen, N. Alharzali, H. K. Al Rawas, S. Taamalli, M. Ribaucour, H. L. Nguyen, A. El Bakali, T. C. Ngo, I. Černušák, F. Louis and D. Q. Dao, *Chemosphere*, 2024, **350**, 141085.
39 H. K. Al Rawas, D. H. Truong, E. Schell, J. Faust, S. Taamalli, M. Ribaucour, A. El Bakali, N. Alharzali, D. Q. Dao and F. Louis, *Environ. Sci.:Processes Impacts*, 2025, **27**, 211–224.
40 H. B. Truong, D. Q. Dao, H. H. Do, V. Van Tran, C. Van Nguyen, I. Rabani and J. Hur, *Chemosphere*, 2024, **366**, 143413.
41 M. J. Frisch, G. W. Trucks, H. B. Schlegel, G. E. Scuseria, M. A. Robb, J. R. Cheeseman, *et al.*, *Gaussian 16 Rev. C.01*, References - Scientific Research Publishing, Wallingford, CT, 2016, **https://www.scirp.org/reference/referencespapers?referenceid=3834728**, accessed 23 July 2025.
42 Y. Zhao and D. G. Truhlar, *Theor. Chem. Acc.*, 2008, **120**, 215–241.
43 P. Shanmugam, G. P. Kuppuswamy, K. Pushparaj, B. Arumugam, A. Sundaramurthy and Y. Sivalingam, *J. Mater. Sci.: Mater. Electron.*, 2022, **33**, 9483–9489.
44 Y. Yan, Q. Yang, Q. Shang, J. Ai, X. Yang, D. Wang and G. Liao, *Chem. Eng. J.*, 2022, **430**, 133174.
45 S. Zhu, X. Li, J. Kang, X. Duan and S. Wang, *Environ. Sci. Technol.*, 2019, **53**, 307–315.
46 J. Wang and S. Wang, *Chem. Eng. J.*, 2020, **401**, 126158.
47 N. P. Rini, Zurnansyah, D. A. Larasati, L. J. Mahardhika, P. D. Jayanti, H. P. Kusumah, N. I. Istiqomah, R. M. Tumbelaka, N. S. Asri, J. Angel, T. Kato, D. Oshima, H. Aliah, A. Kusumaatmaja and E. Suharyadi, *J. Sci.:Adv. Mater. Devices*, 2024, **9**, 100812.

48 L. Settimo, K. Bellman and R. M. A. Knegtel, *Pharm. Res.*, 2014, **31**, 1082–1095.
49 S. Agopcan Cinar, A. Ziylan-Yavaş, S. Catak, N. H. Ince and V. Aviyente, *Environ. Sci. Pollut. Res.*, 2017, **24**, 18458–18469.
50 K. Sehested, H. Corfitzen, H. C. Christensen and E. J. Hart, *J. Phys. Chem.*, 1975, **79**, 310–315.
51 A. Younis, D. Chu, Y. V. Kaneti and S. Li, *Nanoscale*, 2015, **8**, 378–387.
52 E. Raudonyte-Svirbutaviciene, A. Neagu, V. Vickackaite, V. Jasulaitiene, A. Zarkov, C. W. Tai and A. Katelnikovas, *J. Photochem. Photobiol., A*, 2018, **351**, 29–41.
53 Y. Hao, L. Li, J. Zhang, H. Luo, X. Zhang and E. Chen, *Int. J. Hydrogen Energy*, 2017, **42**, 5916–5929.
54 X. Bi, S. Yu, E. Liu, L. Liu, K. Zhang, J. Zang and Y. Zhao, *Colloids Surf., A*, 2020, **603**, 125193.
55 S. Pamidighantam, S. Nakandala, E. Abeysinghe, C. Wimalasena, S. R. Yodage, S. Marru and M. Pierce, *Procedia Comput. Sci.*, 2016, **80**, 1927–1939.
56 N. Shen, Y. Fan and S. Pamidighantam, *J. Comput. Sci.*, 2014, **5**, 576–589.
57 R. Dooley, K. Milfeld, C. Guiang, S. Pamidighantam and G. Allen, *J. Grid Comput.*, 2006, **4**, 195–208.